

**Sintering of 4YSZ ($\text{ZrO}_2 + 4 \text{ mol}\% \text{ Y}_2\text{O}_3$)
nanoceramics for solid oxide fuel cells
(SOFCs), their structure and ionic
conductivity**

Dagfinn Mæland ^a, Crina Suciu ^a, Ivar Wærnhus ^a,
Alex C. Hoffmann ^{b,*},

^a*Prototech AS, P.B. 6034, 5892 Bergen, Norway*

^b*Department of Physics and Technology, University of Bergen, Allegaten 55, 5007
Bergen, Norway*

Abstract

In this work 4YSZ nanoparticles were produced with a variant of the sol-gel method, the particles were sintered using two different heating schemes, and the properties of the resulting pellets investigated. XRD spectra show the crystal structure of the particles to be mainly cubic, and TEM pictures reveal their size to be around 20 nm. The relative densities of the sintered pellets are found with the Archimedes method to lie between 87 and 97% of the theoretical material density, and the grain size, using thermal etching and SEM imaging, found to lie between 0.2 and 5 μm , depending on the sintering temperature and the presence of impurities. The pellets were subjected to electrical impedance spectroscopy making it possible to distinguish the internal crystal and grain boundary impedances due to their different time-constants. With the “brick layer model” the approximate grain boundary thickness

was found to lie between 4 and 8 nm, depending on the sintering conditions and on the presence of impurities. The specific resistances of the grain interiors and the grain boundaries, and the activation energies for ion diffusion in both, are presented. The ionic conductivities of the pellets are compared with literature values, and are found to compare favorably with these, at some temperatures even with data for 8YSZ, which is the standard material used for electrolytes due to its higher ionic conductivity, but which is also mechanically weaker than 4YSZ.

Key words: Grain growth; Grain boundaries; Nanocomposites; Impedance; Solid oxide fuel cells.

Keywords: 4YSZ, nanoparticles, solid oxide fuel cells, sintering temperature, electrical impedance, grain boundaries

1 Introduction

Fuel cells represent a revolutionary technology for power generation by fuel. In conventional electrical power generation the fuel is oxidised spontaneously in an irreversible combustion reaction, recovering the chemical energy in the fuel as heat, which has to be converted first to mechanical and then to electrical energy. In fuel cell-based power generation the oxidation reaction is carried out in an electrochemical cell, keeping the reactants apart and forcing the electron-transfer involved in the reaction to take place through an external circuit, such that most of the chemical energy can be recovered directly as electrical energy.

* Corresponding author

Email address: alex.hoffmann@ifft.uib.no (Alex C. Hoffmann).

The efficiency of conventional power generation is 33–38%, while that of power generation with high-temperature fuel cells may, if also the waste heat is utilized, be 70% or more. Moreover, the oxidation process in fuel cells takes, with the aid of a catalyst, place at temperatures much lower than the flame temperature, and therefore emits negligible NO_x even in high-temperature fuel cells. Fuel cell-based power generation does not emit any particulates or noise either.

It therefore makes sense to invest heavily in research and development of this technology to preserve fossil fuels and protect the environment. This paper is concerned with development of new materials and manufacturing methods for solid oxide fuel cells.

Important challenges in achieving commercialization of this technology are related to:

- reducing the cell internal resistance such that higher current densities can be generated within the cells, and
- improving cell reliability, mitigating material failure or degradation during operation of the cells.

Both of these challenges are related to the cell materials.

Considerable attention has therefore been paid to improving SOFC materials. References [1–11] contain some recent reviews of this work, much of which has been focused on reducing the size of the microstructure of the cell components and therefore of the particles in the powders used to produce the components.

Producing SOFC components from powders consisting of nanoparticles may be advantageous: electrolytes that are thinner, of higher quality and with

a more uniform stress distribution and electrodes with a finer, more stable microstructure and a larger “triple phase boundary” (TPB) may be produced reducing ohmic resistance in the electrolyte and increasing the reaction rate in the electrodes such that cell efficiency may be increased and/or the cell operating temperature may be reduced. Some specific studies of the use of nanoparticles in SOFC production can be found in references [12–18].

To make thin films of YSZ for electrolytes, it is important for the material to be as strong as possible. Some studies have therefore concentrated on YSZ materials with lower doping concentrations than the standard 8%, and we mention some of these in Section 4, where we compare our results with results from the literature. These materials generally have lower ionic conductivity at least at higher temperatures, but have the advantage of being mechanically stronger.

Some of the present authors have recently [19–22] introduced a new, cost-effective and environmentally friendly variant of the sol-gel method, and shown that this method can produce nano-size particles suitable for use in SOFC components. This work takes the next step of sintering these particles to electrolyte materials.

The main objective of this work was to determine whether nanopowders produced by the new process are suitable as raw material for fine-grained SOFC electrolyte materials with good electrical properties. Another objective was to establish the effect of sintering conditions on the conductivity and on the nature of the grain boundaries and the complex impedance of the sintered materials, and to ascertain the effect—if any—of the presence of impurities. Finally we wished to know whether mechanically strong 4YSZ materials pro-

duced in this way can have satisfactory electrical properties for use as SOFC electrolytes.

2 Experimental

4 mol% Y_2O_3 stabilized ZrO_2 (4YSZ) nanopowder was produced by the modified sol-gel method mentioned above. Two powder batches, denoted by B2 and J1, were produced. The B2 batch was produced in a standard way, while the J1 batch was produced with pure organic precursors, and steps were taken to further limit the impurities introduced during its production, such as placing a lid over the powder during calcination to avoid impurities entering from the furnace.

2.1 Chemicals and powder preparation

- Zirconia salt precursor: ZrCl_4 from Sigma-Aldrich. For the B2 powder batch: Technical $\geq 98\%$ (product number: 14612) and for the J1 powder batch: $99.9 + \%$ (metals basis, product number: 357405).
- Ytria salt precursor: $\text{Y}(\text{NO}_3)_3 \times 6\text{H}_2\text{O}$ from Sigma-Aldrich, 99.9% (metals basis, product number: 237957) was used for both powder batches.
- Pectin: For the B2 powder batch: Sigma-Aldrich Pectin from citrus peel, Galacturonic acid $\geq 74\%$ (product number: P9135) and for the J1 powder batch a commercial pectin type purchased from the supermarket (Jam frysepulver Kraft Foods). The latter typically contains around 50% pectin, in sucrose; residues left after combustion indicated that it contained less impurities than pectin from Sigma-Aldrich.
- Sucrose: ordinary food sucrose, purchased from the supermarket (Eldorado

sucrose, Norges gruppen) for both powder batches.

- Nitric acid: from Riedel-de-Haën (HNO_3) $\geq 65\%$ (product number: 30709) for both powder batches.

After drying, the gels were calcined according to the calcination program illustrated in Figure 1. The heating and cooling rates were $200^\circ\text{C}/\text{hr}$, while the holding-times on the plateaus were 1 and 12 hrs, respectively. The lid placed over the J1 powder gave rise to the presence of remnants of organic compounds after calcining, and two additional calcination processes of 6 hrs each were required to obtain a final powder free of organic compounds.

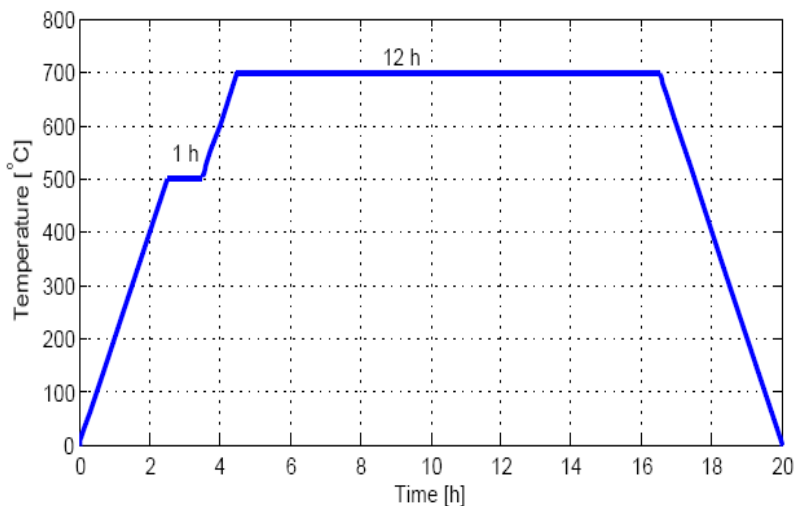


Fig. 1. *Illustration of the calcination program*

After calcination the powder was treated to break down agglomerates. The B2 powder was mortared by hand for 15 minutes. The J1 powder was milled in ethanol for 120 hrs, dried in air at room temperature, and then mortared by hand for one hour. The mill used had a polymer housing, and the milling medium was zirconia balls, while the mortar was made from agate.

Discs were then pressed at approximately 500 bar without binder using a uniaxial press. The discs were then placed in balloons, which were vacuumed and sealed. These balloons were pressed to 1200 bar in a cold isostatic press (CIP). The pressure was held at 1200 bar for 2 minutes before it was slowly lowered. This process did not cause any contamination of the powders. The green density (density before sintering) of the pressed discs was measured, using a caliper to determine the disc volume, before sintering.

2.2 Sintering

The pressed discs were placed on an alumina plate inside the furnace and sintered. The furnace used for sintering was an Entech EEF17 Elevator oven, with a type B thermocouple. Two types of sintering programs were used: referred to as “the one-step program” and “the three-step program”, respectively. Both are illustrated in Figure 2.

The one-step program is the traditional way of sintering. It has one ramp up to a plateau, where the temperature is held constant for a certain period of time, followed by one decline ramp. Different holding temperatures were used to ascertain how the microstructure and the density of the sintered material changed with temperature. The holding times and the slopes of the ramps were the same, 10 hrs and 200°C/hr, respectively, for all the materials sintered by the one-step program.

The three-step sintering program, proposed by Minfang Han et al. [23] was developed to achieve dense sintered bodies with little grain growth. According to Minfang Han et al. [23], the grain growth is a result of grain boundary

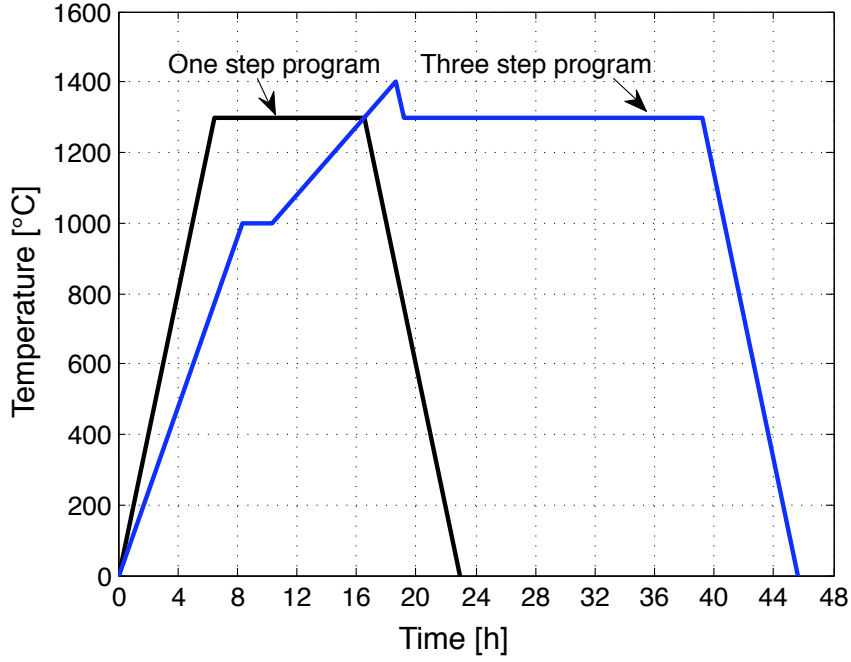


Fig. 2. Sintering programs

motion, which is driven by two processes: grain boundary diffusion and grain boundary migration. Both these processes give rise to densification, but the grain boundary migration gives the most rapid grain growth. So by suppressing grain boundary migration, while keeping grain boundary diffusion active, one can achieve dense sintering with little grain growth. The activation energy for grain boundary diffusion is lower than the activation energy for grain boundary migration. So by keeping the holding plateau at no more than 1300°C, grain boundary migration is suppressed, while grain boundary diffusion is active.

The first ramp of the three-step program had a slope of 120°C/hr and the duration of the first plateau was 2 hrs. The second and third ramps had slopes of 48°C/hr and -200°C/hr, respectively, and the second plateau was held for 20 hrs. The final decline ramp had a slope of -200°C/hr.

2.3 Characterization

The powder batches were analyzed with X-ray diffraction (XRD) to determine the crystal structure and the mean crystallite size. A Bruker D-8 Advance X-ray diffractometer was used for the measurements, and the software Diffract Plus Evaluation (EVA) was used to compare crystal diffraction patterns with those from the International Center for Diffraction Data (ICDD) for identification of the crystal structures. When XRD is performed on powders with random crystal orientation, the diffracted beam is broadened. The extent of this broadening depends on the size of the crystals: it increases with decreasing crystal size. The mean crystallite size can be estimated from the degree of broadening by the empirical Scherrer formula [24]

$$L = \frac{\lambda K}{\beta \cos \theta} . \quad (1)$$

Here L is the mean crystalline size, λ is the wavelength of the X-ray, β is the full width of a peak at half of the maximum of the peak (FWHM) in the diffraction spectra (measured in radians), θ is the Bragg angle and K is a numerical constant equal to 0.9 [25, 26].

The morphology of the powders was investigated by a JEOL-JEM-1011 transmission electron microscope (TEM), while that of the sintered materials was investigated by a ZEISS SUPRA 55VP scanning electron microscope (SEM). Before SEM investigations materials were polished and thermally etched. From the SEM images the grain sizes of the sintered materials were estimated using the lineal intersect method, according to the relation

$$\overline{G} = \frac{1.570}{N_L} . \quad (2)$$

Here \bar{G} is the mean grain size, N_L is the number of counted grains divided by the length of the test line and the constant 1.570 is a dimensionless correction factor [27] accounting for the arbitrary intercepts of the plane and of the test line with respect to the grains.

The relative densities of the sintered pellets were found with the Archimedes method, choosing the theoretical density of 4YSZ to 6050 kg/m³ [28,29], while the relative densities of the green (before sintering) discs were calculated from the mass and dimensions of the pressed discs, the latter were determined using a caliper.

Ionic conductivities of the sintered 4YSZ discs were investigated by impedance spectroscopy. A Solartron analytical 1260 Impedance/Gain-Phase Analyzer was used to obtain the impedance data using a four-wire setup, illustrated in Figure 3. In this setup, wires were welded pairwise to platinum foils and these foils were then brought into contact with the material disc, which was painted with platinum paste on both sides. The setup allowed measurement of the current in the current-carrying circuit containing the voltage generator by measuring the voltage over a standard resistance (not shown, inside the box) incorporated in the circuit. Measurement of the voltage over the pellet was done in a separate circuit as shown, making it possible to eliminate the resistance in the current-carrying circuit in the determination of the voltage over the pellet. The data were analyzed using the complex nonlinear least square (CNLS) program LEVMW, version 8.08. Measurements were performed in the temperature range of 200–1000°C. The signal strength was typically 500 mV at the lower temperatures.

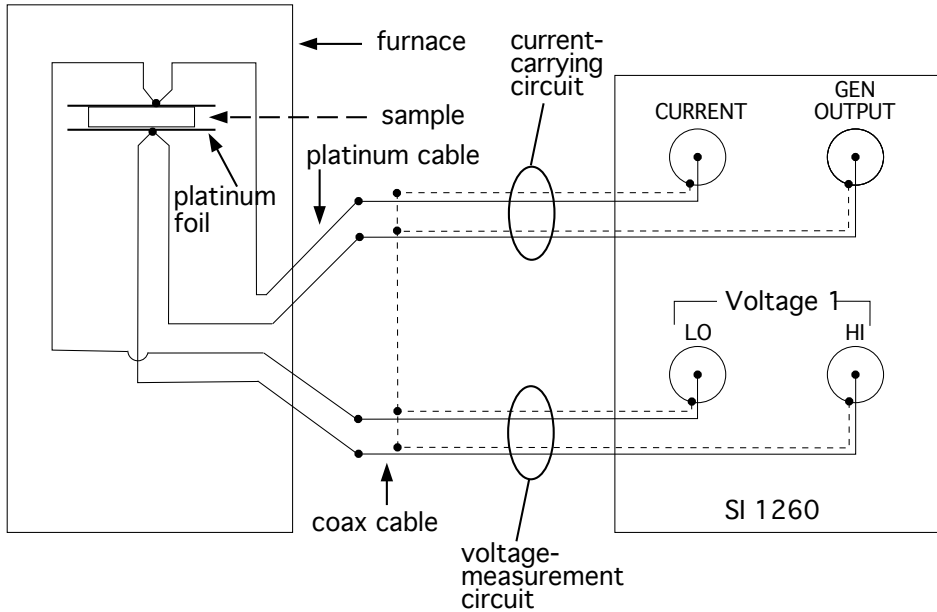


Fig. 3. Principle sketch of the experimental setup for the impedance measurements.

3 Analyses, results and discussion

3.1 Powder characterization

The XRD spectra from the B2 and J1 powders are presented in Figure 4 together with the characteristics of cubic 8YSZ and tetragonal 4YSZ. The samples seem to be mostly cubic, but with some tetragonal phase, evidenced by the asymmetry and slight broadening of the sixth peak in the spectra. The mean crystallite sizes estimated from the first four peaks in the XRD-data, using the Scherrer formula, Equation (1), were 14.82 nm and 10.32 nm for the B2 and J1 samples, respectively.

TEM images of the B2 and J1 sample are shown in Figure 5, showing nanosized particles with a relatively narrow size distribution around a mean size of about 20 nm for both of the samples. The particle size appears somewhat larger than the crystallite size as obtained from the Scherrer formula, indicating that the

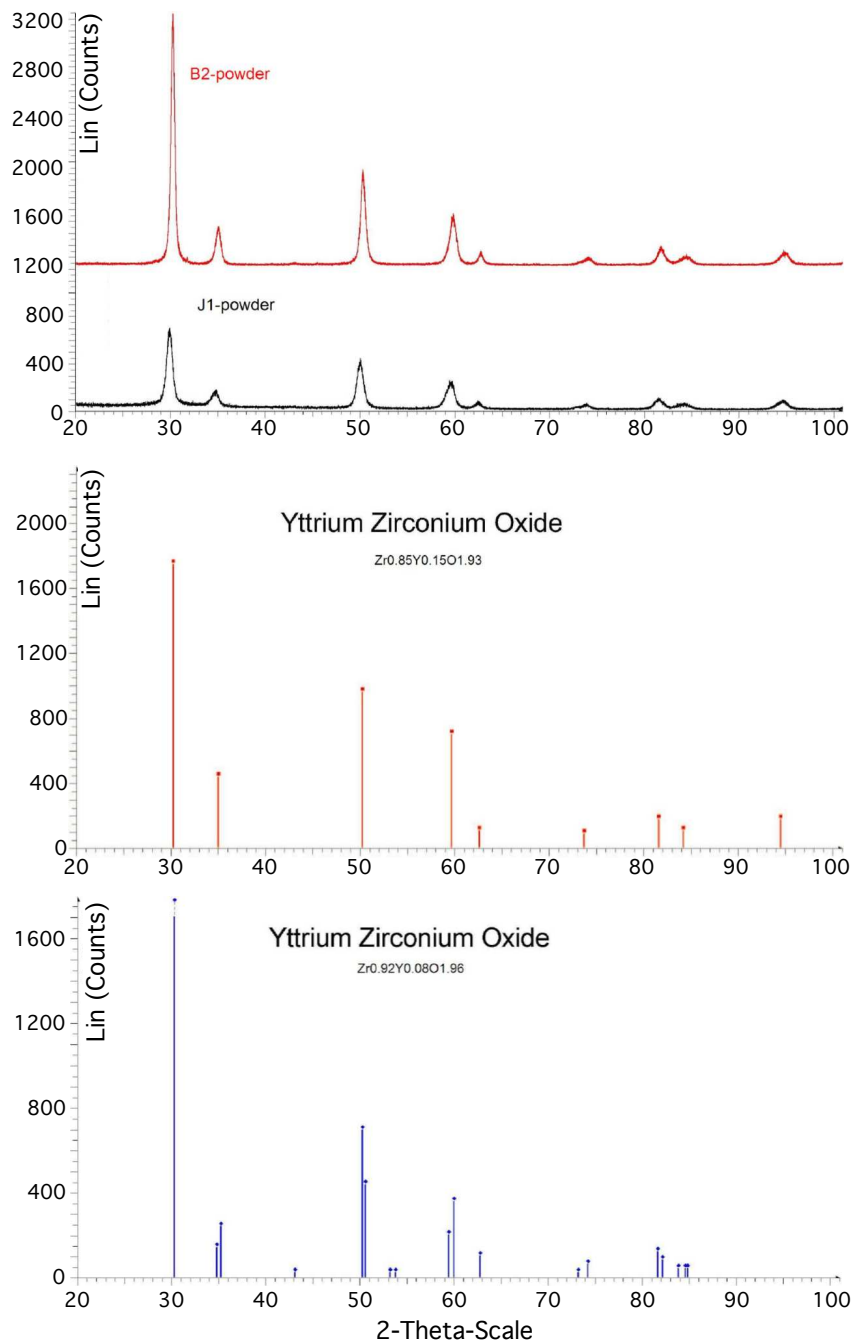


Fig. 4. On the top the XRD spectra for the B2 and J1 sample are shown. The figures in the middle and bottom show the characteristics of cubic 8YSZ and tetragonal 4YSZ, respectively.

particles consist of several crystallites.

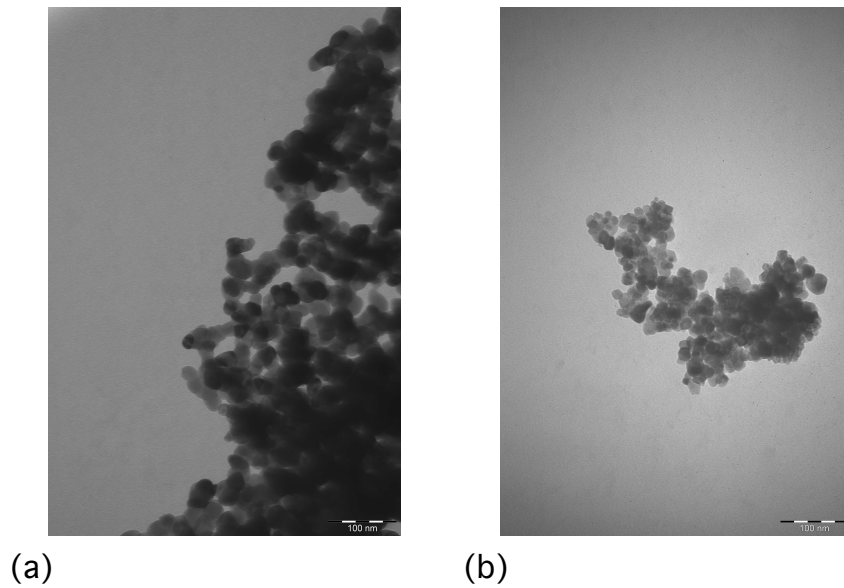


Fig. 5. TEM pictures of (a) the B2 powder and (b) the J1 powder, showing average particle sizes of around 20 nm.

We did not repeat the XRD analysis for the sintered nanoceramics, but their high ionic conductivities (see below) indicate that these must also largely have had a cubic crystal structure.

3.2 Density and grain size of the sintered pellets

Relative green densities were found to be around 0.39 for the B2 samples and to lie in the range 0.44–0.46 for the J1 samples. This difference between the two types of sample is probably due to the difference in treatment of the powders before pressing, where, as mentioned, the B2 powder was only mortared for 15 minutes, while the J1 powder was milled for 120 hrs before being dried and mortared for one hour.

Relative densities and grain sizes of the sintered materials are presented in

Figure 6. These results show a higher sintering activity (higher relative density) for the J1 materials than for the B2 materials, both prepared by the one-step and the three-step programs. This may be due either to the higher green densities or the higher purity of the J1 materials [30,31]. The two plots of grain size in the figure indicate more grain growth for the B2 materials. This may be due to the lower green packing density of the B2 materials [32].

The sintering results for the materials sintered by the three-step program confirm the contention that a higher density with little grain growth is achieved by this sintering program [23]. The closeness of the results from the three B2 materials sintered by the three-step program is evidence of good repeatability of the sintering results. Note that the grain size was only investigated for one of these three materials, namely the one with the intermediate relative density of 0.954 (see the top left-hand plot in Figure 6).

3.3 Oxygen ion conductivity

Ionic conductivity can be investigated by complex impedance spectroscopy [33]. The impedance, Z , is normally a function of frequency, ω . The impedance is investigated during the measurement at a wide range of frequencies, typically between 1 MHz to 1 mHz, which was also the range used in this study, yielding the impedance function $Z(\omega)$. This impedance function may in turn be assigned to an equivalent electrical circuit, where different physical processes are represented by the elements of the equivalent electrical circuit and can thus be distinguishable. To do this the parameters of the elements of the equivalent electrical circuit are fitted so that the impedance of the equivalent electrical circuit matches that of the material.

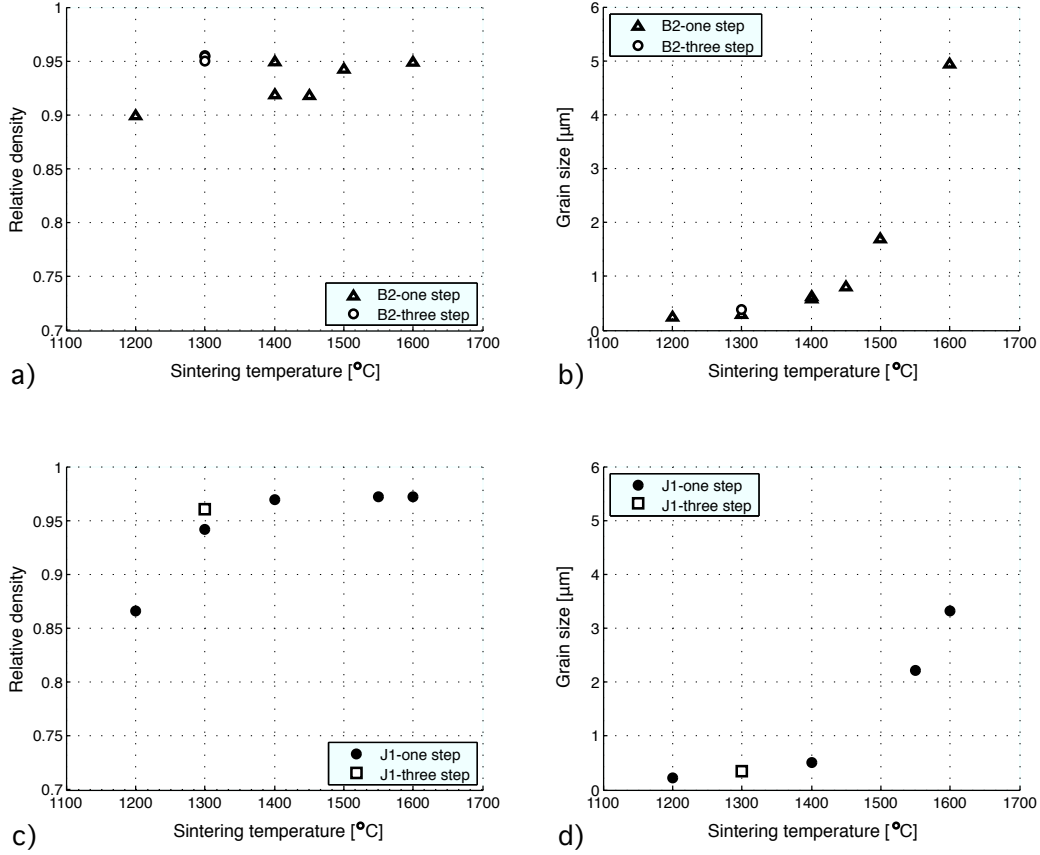


Fig. 6. Relative densities and grain sizes for materials subjected to different sintering treatments.

For the type of material we are considering in this paper the equivalent electrical circuit may consist of a resistive element, with impedance $Z(\omega) = R$, simulating ohmic resistance in the material, in parallel with a capacitor, with impedance $Z(\omega) = 1/j\omega C$ where j is the imaginary number and C the capacitance, to simulate dielectric effects in the material. A polycrystalline material may be represented by two such parallel-coupled resistor/capacitor pairs in series, one to represent the grain interior and the other to represent the grain boundary regions. If the time constants, RC , of these two pairs are sufficiently different, the characteristic response time of the two will be different, and the complex impedance, $Z(\omega)$ will trace out two distinct semicircles in the complex plane, one representing the characteristics of the grain boundary region

and the other representing the characteristics of the grain interior region. We have to refer to a textbook on electrical impedance analysis (e.g. ref. [33]) for an account of this.

In our case it turned out that $Z(\omega)$ traced out slightly depressed semicircles. This is often the case, and can be accounted for by replacing the capacitors in the equivalent electrical circuit by “constant phase elements” with the impedance function $Z_{CPE} = \frac{1}{Y(j\omega)^n}$, which reduces to that of a capacitor for $n = 1$.

The equivalent electrical circuit chosen in the end for this work is shown in Figure 7. The inductor, L , and the Generalized Finite Warburg element, GFW, are included to account for the responses of the wiring and the electrodes, respectively, and are not relevant for this study. However, the response function of the latter: $Z_{GFW} = R_{GFW} \tanh\left(\frac{(jT\omega)^n}{(jT\omega)^n}\right) / (jT\omega)^n$ [34] is included in the fit procedure to obtain a good fit for the grain boundary response.

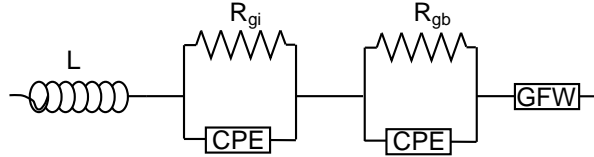


Fig. 7. equivalent electrical circuit chosen at low temperatures. L is an inductor accounting for the response of the wiring, R_{gi} the grain interior resistance, R_{gb} the grain boundary resistance, CPE are constant phase elements representing dielectric effects in the two regions, and GFW is the Generalized Finite Warburg [34] which accounts for the response of the electrodes.

Figure 8 shows impedance plots for three of the materials: one B2 material sintered by the three-step program, the J1 material sintered by the three-step

program and the J1 material sintered at 1550°C by the one-step program. ρ is impeditivity: $\rho \equiv (ZA)/t$, where A is the cross-sectional area and t is the thickness of the pellet, such that the real part of ρ is the bulk resistivity of the polycrystalline material. The reciprocal of ρ is the material conductivity, which we denote by σ . In the impedance plots the semicircle to the left arises from grain interior response, which has the lowest time constant and the lowest capacitance in the equivalent electrical circuit, and the right semicircle is due to the grain boundary response. By using a complex nonlinear least square (CNLS) fitting program the resistivities and the CPE parameters are estimated.

The figure shows that the response of the grain interiors are similar for the three materials, as one would expect, and the difference lies in the response of the grain boundaries, where the grain boundary impeditivity of the B-material is much greater than those of the J-materials. The reason that the grain boundary impeditivity is lower in the one-step material than in the three-step material is that the sintering temperature and the densification of the former was larger than for the latter (see the bottom left-hand plot in Figure 6). It is likely that for the same sintering temperature the impeditivity of the three-step material will be lower than that of the one-step material.

Figure 9 shows the impeditivity of the B2-three step material together with the CNLS fitted response of the equivalent electrical circuit shown in Figure 7. The circuit chosen is clearly sufficient to reflect the physical processes taking place in the material.

On basis of the impeditivity plots and the fitted equivalent electrical circuits the total conductivity and the separate grain interior and grain boundary

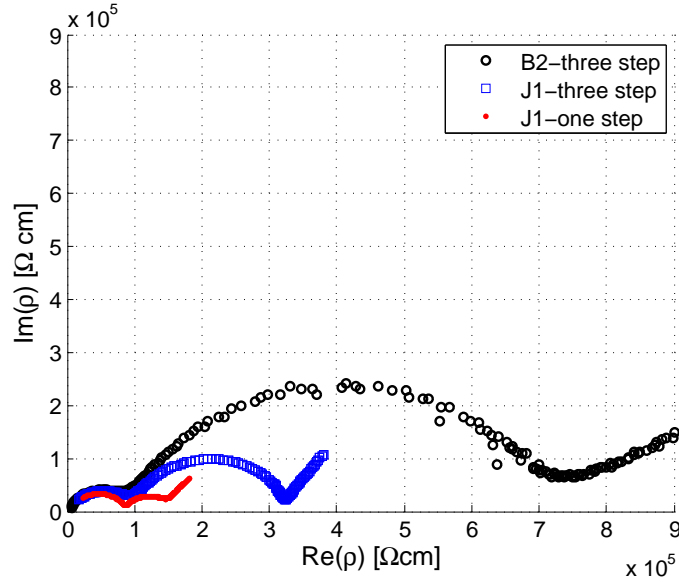


Fig. 8. Plot of the impedivity of three materials at approximately 300°C .

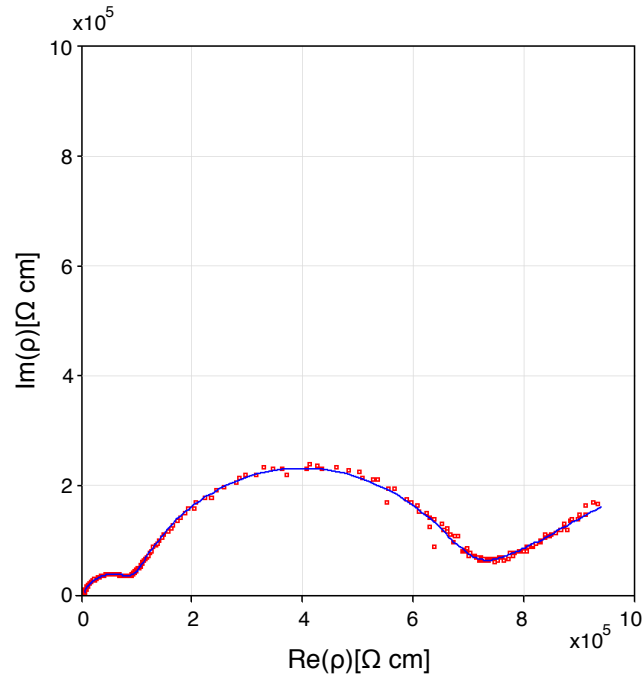


Fig. 9. Impedance results for the B2-three step material with the fitted response of the equivalent electrical circuit shown in Figure 7.

conductivities can be determined. The corresponding resistivities are given by the intersections of the impedance semicircles with the $\text{Re}(\rho)$ axis; values of resistivities are evaluated by means of the mentioned fitting program.

Ionic conductivity of YSZ is a thermally activated process, and the conductivity may be expressed by the known Arrhenius dependence [33, 35]

$$\sigma = \frac{E}{T} \exp\left(-\frac{A}{kT}\right). \quad (3)$$

Here σ is the conductivity, E is a constant, A is the activation energy, k is the Boltzmann constant, and T is the absolute temperature.

The conductivity plots in Figure 10 confirm that in the measured temperature range, the bulk conductivities, σ , of grain interiors are very similar, whereas the conductivities of grain boundaries are significantly different for all three systems investigated.

The activation energies of the different processes, calculated according to Equation (3) can be determined from the slopes in these plots. These activation energies are given in Table 1 below.

Using the estimated equivalent electrical circuit parameters obtained from the CNLS fitting program, some microstructural properties can be estimated using the so-called “brick-layer model”, which is based on assuming a regular arrangement of cubic grains separated by planar grain boundaries [33] like bricks in a wall separated by cement.

In the following we operate with conductivity contributions from two “regions”: a contribution from the grain interior region and a contribution from the the grain boundary region, denoted by subscript gi and gb , respectively. We denote by σ_{gi} and σ_{gb} the reciprocals of the contributions of the two regions, respectively, to the over-all resistivity of the material, e.g. σ_{gb} is thus the bulk, or “macroscopic”, conductivity of the grain boundary region. We denote by g_{gi} and g_{gb} , respectively, the reciprocals of the resistivities of the

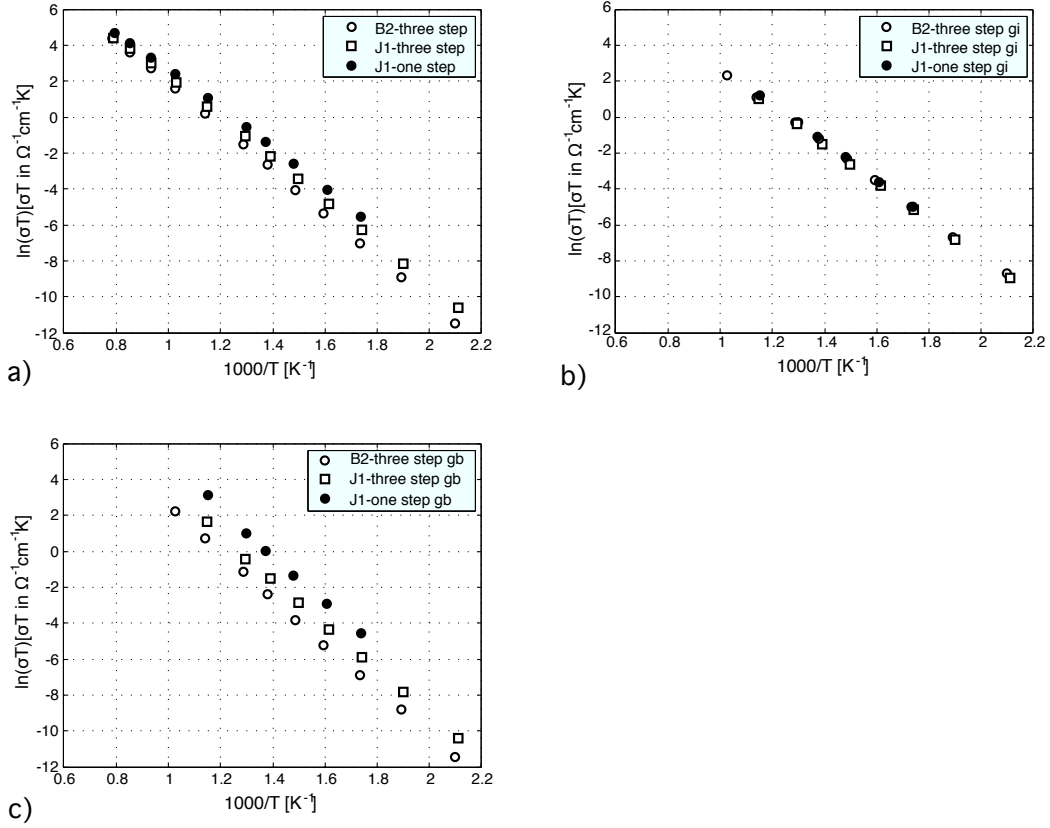


Fig. 10. Modified Arrhenius plots for the conductivities of a) the total material, b) the grain interiors and c) the grain boundaries

two pure regions, e.g. g_{gb} is thus the “microscopic” conductivity of the pure grain boundary region.

When applying the brick layer model we assumed that:

- The conductivity of the grain interior region was much greater than the conductivity of the grain boundary region, $g_{gi} \gg g_{gb}$.
- The permittivity of the grain interior region was equal to the permittivity of the grain boundary region, $\epsilon_{gi} = \epsilon_{gb}$.

The former assumption is often used for polycrystalline ion conducting YSZ, which shows two semicircles in the impedance plot [31, 36–38], and the latter is appropriate since the material permittivity does not vary much compared

with the conductivity [33, 39].

The volume fraction of grain boundary region is in this simplified grain arrangement is:

$$x_{gb} = \frac{3D^2d}{3D^2d + D^3} \approx \frac{3d}{D}, \quad (4)$$

where d is the grain boundary thickness and D is the grain size. The approximation holds for $D \gg d$.

We must refer to a textbook [33] for the derivation of the following relations under the assumptions given above. The thickness of the grain boundary region can be shown to be

$$d = \frac{Dc_{gi}}{c_{gb}}. \quad (5)$$

where c are effective capacitances determined for the CPE elements in the equivalent electrical circuit in Figure 7.

The fractional conductivity of the grain boundary region can be shown to be:

$$\frac{g_{gb}}{g_{gb} + g_{gi}} = \frac{\sigma_{gb}x_{gb}}{\sigma_{gb}x_{gb} + 3\sigma_{gi}}. \quad (6)$$

Estimates based on the brick layer model and the measured parameters are presented in Table 1.

The grain boundaries can be seen in the table to be much narrower in the pure materials. The activation energies for conductivity are very similar between all the materials for both regions. The 90% confidence intervals for the activation energies are approximately ± 0.01 eV.

Table 1

Calculated parameters using the modified Arrhenius plots and the brick layer model.

material	gb thickness	$\frac{g_{gb}}{g_{gb}+g_{gi}}$	x_{gb}	A_{total}	A_{gi}	A_{gb}
	[nm]			[eV]	[eV]	[eV]
B2-three step	8.22	0.00320	0.0632	1.04	0.89	1.10
J1-three step	4.71	0.00610	0.0389	0.98	0.90	1.07
J1-one step (1550°C)	4.00	0.00271	0.00543	0.93	0.91	1.12

4 Comparison with Literature and Further Discussion

Since the goal of this investigation was to test whether materials produced with the present process are suitable for use in solid oxide fuel cells and are comparable in performance with the materials presently on the market, we have carried out a search and collected some literature data on the performance of similar materials for comparison with the results shown above.

Table 2 shows results for the total, i.e. bulk plus grain boundary, conductivity of the J1-1550 sample from the present investigation, determined from the complex impedance plots, and Table 3 shows a collection of results for other YSZ materials with varying degree of doping. In this table, the result marked with * is interpolated between 799.8°C and 899.3°C and those marked ** have been annealed at 1000°C for 5000 min.

It is seen that the conductivity of the best material produced in the present work is fully as good as, or better than, comparable materials and, at lower temperatures (600°C), even as good as literature data for 8YSZ materials.

Table 2

Conductivity [$\Omega^{-1}\text{cm}^{-1}$] for the J1-one step material, this work

Temperature	497.8°C	596.7°C	799.8°C	850°C	899.3°C	989.8°C
J1-1550	7.450E-4	3.315E-3	0.0257	0.037*	0.0512	0.0881

Table 3

Literature values for conductivities of YSZ [$\Omega^{-1}\text{cm}^{-1}$]

Temperature	500°C	600°C	800°C	850°C	900°C	1000°C
3YSZ	7.4E-5 [40]			0.022** [41]		0.075 [42] 0.059 [43]
4YSZ		~1E-4 [44]		0.024** [41]		
4.3YSZ	~1E-3 [45]					
4.5YSZ	1.2E-5 [40]				0.012 [46]	0.023 [46]
8YSZ		1.587E-3 [47]	0.022 [48]	0.037 [48]		0.089 [42] 0.154 [49]
			0.0185 [47]			
			0.050 [50]			
			0.020 [51]			
			0.0131 [38]			
9YSZ	4.6E-4 [52]					0.13 [43]
9.2YSZ	~1E-3 [45]					0.13 [43]

Table 4 shows activation energies for conductivity in various YSZ materials from the literature, the references are given by each value. The values are consistent with the ones presented here. The values marked with ** have been

annealed at 1000°C for 5000 minutes. The values marked with # refer to clean 8YSZ, this reference also contain values for silica contaminated materials.

Table 4

Activation energies for YSZ materials from literature.

Material	A_{gi} [eV]	A_{gb} [eV]	A_{tot} [eV]
3YSZ	0.73 [53]	1.24 [53]	0.97 [53]
	0.97 [40]	1.21 [40]	1.12 [40]
	0.98 [54]	1.12 [54]	
	0.92 [54]	1.09 [54]	
4YSZ			0.94** [41]
4.5YSZ	1.12 [40]	1.27 [40]	1.27 [40]
4.7YSZ	1.07 [54]	1.15 [54]	
6YSZ	1.07 [54]	1.12 [54]	
	1.02 [40]	1.20 [40]	1.18 [40]
8YSZ	0.90 [53]	1.15 [53]	0.96 [53]
	1.11-1.17# [31]	1.11-1.25# [31]	
	1.04-1.07 [55]	1.21-1.23 [55]	
			1.00 [56]
		0.91-0.96 [41]	

Martin and Mecartney [31], studied the grain boundary thickness as a function

of sintering temperature and the amount of Si-based impurities present in the material. Comparing their data with the data in Table 1 we see that our grain boundary thicknesses are comparable to the ones obtained for the pure materials in that work, and our trends consistent with theirs, confirming the validity of our analysis method.

We discuss briefly the validity and limitations of the brick-layer model. The properties of the grain interior are often well determined by this model [57]. But the grain boundary properties may be less well estimated. A wide grain size distribution, or a bimodal grain size distribution, may cause the current to take detours around small grains, or clusters of small grains [37,57], causing the estimated grain boundary resistance to be too low. Fleig and Maier [58], Fleig [37], and Dezanneau et al. [59] have simulated impedance response for idealized 2-D periodic grain structures (identical grain size, and shape), more realistic 2-D microstructures (differently shaped grains with a size distribution), and realistic 3-D microstructures (differently shaped grains with a size distribution), respectively for which the true material parameters for the grain interior phase, and the grain boundary phase were known. The estimated parameters for the grain boundary properties using the brick layer model agreed with the real parameters to within 10%.

5 Concluding Remarks

We conclude from the previous sections, specifically after comparison of the data in Tables 2 and 3, that the manufacturing methods presented in this work, which are cost-effective and environmentally friendly, can result in fine-grained materials that have electrochemical properties that are at least comparable to

the ones reported in the literature. We also conclude that 4YSZ materials produced by the present variant of the sol-gel method seem suitable for use as electrolytes in solid oxide fuel cells.

Sintering densities of about 96% and 97% of the theoretical density could be reached for J1 materials, either by sintering according to the three-step program, or by sintering at temperatures over 1400°C . This batch shows good sintering activity. A combination of residual agglomerates leading to poor packing, and impurities is probably the reason that the B2 powder had less sintering activity.

The work confirms that impurities have an important negative effect on the conductivity of 4YSZ. This effect is seemingly due to segregation of impurities into the grain boundaries, since the grain interior conductivities are equal for all the materials. The grain boundary thickness was reduced from 8 nm to 4 nm from the B2 to the purer J1 materials.

6 Acknowledgments

This work was funded by the NFR (Norwegian Research Council) and Prototech A.S., Bergen, Norway. Also, the authors are grateful to the group of Professor Karl Törnroos at the Chemistry Institute, University of Bergen, Norway for their help with the XRD measurements and Egil Erichsen at the electron microscope at the University of Bergen.

References

- [1] K. Kendall, Progress in solid oxide fuel cell materials, *International Materials Reviews* 50 (2005) 257–264.
- [2] J. B. Lu, Z. T. Zhang, Z. L. Tang, Review on the development of solid oxide fuel cells, *Rare Metal Materials and Engineering* 34 (2005) 1177–1180.
- [3] P. Holtappels, U. Vogt, T. Graule, Ceramic materials for advanced solid oxide fuel cells, *Advanced Engineering Materials* 7 (2005) 292–302.
- [4] R. S. Amado, L. F. B. Malta, F. M. S. Garrido, M. E. Medeiros, Solid oxide fuel cells: Materials, components and configurations., *Quimica Nova* 30 (2007) 189–197.
- [5] J. W. Fergus, Electrolytes for solid oxide fuel cells, *Journal of Power Sources* 162 (2006) 30–40.
- [6] J. W. Fergus, Oxide anode materials for solid oxide fuel cells, *Solid State Ionics* 177 (2006) 1529–1541.
- [7] E. V. Tsipis, V. V. Kharton, Electrode materials and reaction mechanisms in solid oxide fuel cells: a brief review, *Journal of Solid State Electrochemistry* 12 (2008) 1367–1391.
- [8] E. V. Tsipis, V. V. Kharton, Electrode materials and reaction mechanisms in solid oxide fuel cells: a brief review, *Journal of Solid State Electrochemistry* 12 (2008) 1039–1060.
- [9] J. B. Goodenough, Y. H. Huang, Alternative anode materials for solid oxide fuel cells, *Journal of Power Sources* 173 (2007) 1–10.
- [10] A. Atkinson, B. Sun, Residual stress and thermal cycling of planar solid oxide fuel cells, *Materials Science and Technology* 23 (2007) 1135–1143.

- [11] C. W. Sun, U. Stimming, Recent anode advances in solid oxide fuel cells, *Journal of Power Sources* 171 (2007) 247–260.
- [12] V. Esposito, D. Z. de Florio, F. C. Fonseca, E. N. S. Muccillo, R. Muccillo, E. Traversa, Electrical properties of YSZ/NiO composites prepared by a liquid mixture technique, *Journal of the European Ceramic Society* 25 (2005) 2637–2641.
- [13] Y. Sunagawa, K. Yamamoto, A. Muramatsu, Improvement in SOFC anode performance by finely-structured Ni/YSZ cermet prepared via heterocoagulation, *Journal of Physical Chemistry B* 110 (2006) 6224–6228.
- [14] G. Q. Xie, M. F. Luo, M. He, P. Fang, Y. F. Ying, Z. L. Yan, An improved method for preparation of $\text{Ce}_{0.8}\text{Pr}_{0.2}\text{O}_Y$ solid solutions with nanoparticles smaller than 10 nm, *Journal of Nanoparticle Research* 9 (2007) 471–478.
- [15] R. Habermann, T. Fukui, Optimized performance of nanoparticle composites for solid oxide fuel cells by a new generation of powder processor, *CFI-Ceramic Forum International* 84 (2007) E14+.
- [16] T. Z. Sholklapper, V. Radmilovic, C. P. Jacobson, S. J. Visco, L. C. de Jonghe, Synthesis and stability of a nanoparticle-infiltrated solid oxide fuel cell electrode, *Electrochemical and Solid State Letters* 10 (2007) B74–B76.
- [17] T. van Gestel, D. Sebold, W. A. Meulenbergh, H. P. Buchkremer, Development of thin-film nano-structured electrolyte layers for application in anode-supported solid oxide fuel cells, *Solid State Ionics* 179 (2008) 428–437.
- [18] M. Tahmasebpour, A. A. Babaluo, M. K. R. Aghjeh, Synthesis of zirconia nanopowders from various zirconium salts via polyacrylamide gel method, *Journal of the European Ceramic Society* 28 (2008) 773–778.
- [19] C. Suci, A. C. Hoffmann, P. Kosinski, Obtaining YSZ nanoparticles by the sol-gel method with sucrose and pectin as organic precursors, *Journal of Materials*

Processing Technology 202 (2008) 316–320.

- [20] C. Suci, L. Gagea, A. C. Hoffmann, M. Mocean, Sol-gel production of zirconia nanoparticles with a new organic precursor, *Chemical Engineering Science* 61 (2006) 7831–7835.
- [21] C. Suci, A. C. Hoffmann, A. Vik, F. Goga, Effect of calcination conditions and precursor proportions on the properties of YSZ nanoparticles obtained by modified sol-gel route, *Chemical Engineering Journal* 138 (2008) 608–615.
- [22] C. Suci, A. C. Hoffmann, E. Dorolti, R. Tetean, NiO/YSZ nanoparticles obtained by new sol-gel route, *Chemical Engineering Journal* 140 (2008) 586–592.
- [23] M. F. Han, X. L. Tang, H. Y. Yin, S. P. Peng, Fabrication, microstructure and properties of a YSZ electrolyte for SOFCs, *Journal of Power Sources* 165 (2007) 757–763.
- [24] A. L. Patterson, The Scherrer formula for X-ray particle size determination, *Physical Review* 56 (1939) 978.
- [25] C. Brahim, A. Ringuede, M. Cassir, M. Putkonen, L. Niinisto, Electrical properties of thin yttria-stabilized zirconia overlayers produced by atomic layer deposition for solid oxide fuel cell applications, *Applied Surface Science* 253 (2007) 3962–3968.
- [26] J. T. Abiade, G. X. Miao, A. Gupta, A. A. Gapud, D. Kumar, Structural and magnetic properties of self-assembled nickel nanoparticles in a yttria stabilized zirconia matrix, *Thin Solid Films* 516 (2008) 2082–2086.
- [27] M. Mendelson, Average grain size in polycrystalline ceramics, *Journal of The American Ceramic Society* 52 (1969) 443–446.
- [28] B.-K. Jang, H. Matsubara, Influence of porosity on thermophysical properties

of nano-porous zirconia coatings grown by electron beam-physical vapor deposition, *Scripta Materialia* 54 (2006) 1655–1659.

- [29] M. Kuwabara, T. Murakami, M. Ashizuka, Y. Kubota, T. Tsukidate, Electrical conductivity of yttria partially stabilized zirconia ceramics, *Journal of Materials Science Letters* 4 (1985) 467–471.
- [30] T. S. Zhang, J. Ma, Y. Z. Chen, L. H. Luo, L. B. Kong, S. H. Chan, Different conduction behaviors of grain boundaries in SiO₂-containing 8YSZ and CGO20 electrolytes, *Solid State Ionics* 177 (2006) 1227–1235.
- [31] M. C. Martin, M. L. Mecartney, Grain boundary ionic conductivity of yttrium stabilized zirconia as a function of silica content and grain size, *Solid State Ionics* 161 (2003) 67–79.
- [32] R. M. German, *Sintering Theory and Practice*, WILEY, 1996.
- [33] E. Barsoukov, J. R. Macdonald (Eds.), *Impedance Spectroscopy Theory, Experiment, and Application*, 2nd Edition, WILEY, Hoboken, 2005.
- [34] R. Macdonald, *LEVM / LEVMW Manual*, Solartron Group, version 8.08 Edition (February 2007).
- [35] J. B. Goodenough, Oxide-ion electrolytes, *Annual Review of Materials Research* 33 (2003) 91–128.
- [36] X. Guo, W. Sigle, J. Fleig, J. Maier, Role of space charge in the grain boundary blocking effect in doped zirconia, *Solid State Ionics* 154-155 (2002) 555–561.
- [37] J. Fleig, The grain boundary impedance of random microstructures: numerical simulations and implications for the analysis of experimental data, *Solid State Ionics* 150 (2002) 181–193.
- [38] Y. Liu, L. E. Lao, Structural and electrical properties of ZnO-doped 8 mol% yttria-stabilized zirconia, *Solid State Ionics* 177 (2006) 159–163.

- [39] S. Haile, D. West, J. Campbell, The role of microstructure and processing on the proton conducting properties of gadolinium-doped barium cerate, *Journal of Materials Research* 13 (1998) 1576–1595.
- [40] R. Ramamoorthy, D. Sundararaman, S. Ramasamy, Ionic conductivity studies of ultrafine-grained yttria stabilized zirconia polymorphs, *Solid State Ionics* 123 (1999) 271–278.
- [41] S. P. S. Badwal, F. T. Ciacchi, K. M. Giampietro, V. Lawrie, S. R. D., Zirconia-yttria electrolyte materials for solid oxide fuel cells, *EUR SOFC Forum* (2002) 199–206.
- [42] A. J. Feighery, J. T. S. Irvine, Effect of alumina additions upon electrical properties of 8 mol.% yttria-stabilised zirconia, *Solid State Ionics* 121 (1999) 209–216.
- [43] K. Kendall, S. C. Singhal, *High temperature solid oxide fuel cells: fundamentals, design, and applications*, Elsevier, Oxford, 2003.
- [44] Y. Y. Chen, W. C. J. Wei, Processing and characterization of ultra-thin yttria-stabilized zirconia (YSZ) electrolytic films for SOFC, *Solid State Ionics* 177 (2006) 351–357.
- [45] M. Hartmanova, J. Schneider, V. Navratil, F. Kundracik, H. Schulz, E. E. Lomonova, Correlation between microscopic and macroscopic properties of yttria stabilized zirconia 1. single crystals, *Solid State Ionics* 136 (2000) 136–137.
- [46] X.-J. Ning, C.-X. Li, C.-J. Li, G.-J. Yang, Effect of powder structure on microstructure and electrical properties of plasma-sprayed 4.5 mol% YSZ coating, *Vacuum* 80 (2006) 1261–1265.
- [47] R. S. Gordon, Ion conducting ceramic electrolytes: A century of progress, *Proc., Electrochem. Soc.* 07 (2003) 141–151.

- [48] T. He, Q. He, N. Wang, Synthesis of nano-sized YSZ powders from glycine-nitrate process and optimization of their properties, *Journal of Alloys and Compounds* 396 (2005) 309–315.
- [49] M. Mori, M. Yoshikawa, H. Itoh, T. Abe, Effect of alumina on sintering behavior and electrical conductivity of high-purity yttria-stabilized zirconia, *Journal of the American Ceramic Society* 77 (1994) 2217–2219.
- [50] T. Corporation, http://www.tosoh.com/products/bs+basic2_grades.htm (2008).
- [51] FCM, <http://www.fuelcellmaterials.com/pdf/Zirconias%205-9-2006.pdf>.
- [52] A. M. Azad, S. Larose, S. A. Akbar, Bismuth oxide-based solid electrolytes for fuel-cells, *Journal of Materials Science* 29 (1994) 4135–4151.
- [53] T.-H. Yeh, C.-C. Chou, Doping effect and vacancy formation on ionic conductivity of zirconia ceramics, *Journal of Physics and Chemistry of Solids* In Press, Corrected Proof.
- [54] N. Bonanos, R. K. Slotwinski, B. C. H. Steele, E. P. Butler, High ionic conductivity in polycrystalline tetragonal Y₂O₃ ZrO₂, *Journal of Materials Science Letters* 3 (1984) 245–248.
- [55] M. Ali, O. A. Abdelal, A. A. Hassan, Impedance spectroscopy of YSZ electrolyte containing CuO for various applications, *Solid State Ionics* 178 (2007) 1463–1466.
- [56] E. Ramirez, A. Huanosta, J. P. Sebastian, L. Huerta, A. Ortiz, J. C. Alonso, Structure, composition and electrical properties of YSZ films deposited by ultrasonic spray pyrolysis, *Journal of Materials Science* 42 (2007) 901–907.
- [57] J. Fleig, J. Maier, The impedance of ceramics with highly resistive grain boundaries: validity and limits of the brick layer model, *Journal of the European Ceramic Society* 19 (1999) 693–696.

- [58] J. Fleig, J. Maier, A finite element study on the grain boundary impedance of different microstructures, *Journal of the Electrochemical Society* 145 (1998) 2081–2089.
- [59] G. Dezanneau, A. Morata, A. Tarancon, F. Peiro, J. R. Morante, Effect of grain size distribution on the grain boundary electrical response of 2d and 3d polycrystals, *Solid State Ionics* 177 (2006) 3117–3121.